The Astrophysical Journal, 926:93 (9pp), 2022 February 10 https://doi.org/10.3847/1538-4357/ac3cbd

Ultraviolet Observations of Comet 96/P Machholz at Perihelion

J. C. Raymond[1], S. Giordano[2], S. Mancuso[2], Matthew S. Povich[3], and A. Bemporad[2]
[1] Harvard-Smithsonian Center for Astrophysics, 60 Garden St., Cambridge, MA 02138, USA
[2] INAF-Osservatorio Astrofisico di Torino, via Osservatorio 20, I-10025, Pino Torinese, Italy
[3] Department of Physics and Astronomy, California State Polytechnic University, 3801 West Temple Ave., Pomona, CA 91768, USA
Received 2021 November 1; revised 2021 November 22; accepted 2021 November 22; published 2022 February 16

Abstract

Ultraviolet spectra of Comet 96/P Machholz were obtained during its 2002 perihelion with the UltraViolet Coronagraph Spectrometer instrument on board the SOHO satellite. Emission from H I, C II, C III, and O I is detected near the nucleus. The outgassing rate is in line with the value extrapolated from rates at larger distances from the Sun, and abundances of C and O are estimated. Reconstructed images show a nearly spherical cloud of H I Lyα emission and an ion tail seen in C III. Radiation pressure on the hydrogen atoms produces a modest distortion of the shape of the Lyα cloud as seen from SOHO and Doppler shifts up to 30 km s^{-1} in the outer parts of the cloud. We estimate a ratio of C to H_2O similar to what is observed in other comets, so low carbon abundance does not account for the anomalously low C_2 and C_3 ratios to NH_2 observed at optical wavelengths.

Unified Astronomy Thesaurus concepts: Main-belt comets (2131); Comet tails (274); Ultraviolet astronomy (1736); Comet volatiles (2162)

1. Introduction

Comet 96P/Machholz (hereafter Comet Machholz) is remarkable in many ways. It has a very small perihelion distance of 0.124 au and a period of 5.3 yr. Its inclination is high at 58°, but the orbit is changing rapidly. Its eccentricity and inclination oscillate out of phase, with perihelion varying between 0.03 and 1 au on a 4000 yr timescale (Green et al. 1990; McIntosh 1990). Comet Machholz is believed to be the largest surviving piece of a larger body that broke up to produce the Marsden and Kracht groups of sungrazing comets (Ohtsuka et al. 2003) and the Quadrantid (McIntosh 1990) and Na-poor Southern δ Aquarid (Matlovič et al. 2019) meteor streams. It shows remarkably low C_2 and C_3 abundances relative to NH_2 (Langland-Shula & Smith 2007; Schleicher 2008).

Eisner et al. (2019) observed Comet Machholz far from perihelion, when there was no detectable dust coma and they could observe the comet's surface. They found that the colors are unusually blue compared to Jupiter-family comets, its radius is 3.4 km, and it has an axial ratio of 1.6 with a 4.1 hr rotation period. Combi et al. (2011, 2019) reported water production rates of 5×10^{27}–5×10^{29} at distances between 0.16 and 0.83 au.

Because Comet Machholz passes close to the Sun, it presents a good example of dust scattering at extreme phase angles (Grynko et al. 2004). Comet Machholz is expected to be an excellent target for imaging observations at Lyα and white light by the Metis coronagraph on the Solar Orbiter (Bemporad et al. 2015), because from the point of view of the Solar Orbiter, it will transit the Sun in 2023 January (G. Jones & M. Knight 2021, private communication). Thus, it will be seen at an extreme phase angle, and at the same time, it will have a very large outgassing rate.

The UltraViolet Coronagraph Spectrometer (UVCS) on board the SOHO satellite (Kohl et al. 1995) obtained UV spectra of a number of comets, including sungrazing comets (Raymond et al. 1998, 2018; Uzzo et al. 2001; Bemporad et al. 2005; Ciaravella et al. 2010; Giordano et al. 2015; Raymond & Giordano 2019). Those observations were used to determine outgassing rates, dust vaporization rates, and elemental compositions including the products of vaporized dust, along with properties of the solar corona including density, temperature, and outflow speed (Bemporad et al. 2007; Jones et al. 2018). The UVCS also observed the near-Sun comet C1997/H2 (Mancuso 2015) to determine its outgassing rate and the periodic comets Encke (Raymond et al. 2002) and Kudo–Fujikawa (Povich et al. 2003). These observations were used to study outgassing rates, elemental compositions, and the behavior of the ion tail.

The UVCS observed Comet Machholz during its 2002 perihelion. We analyze those observations to determine the composition of the comet and its outgassing rate and study the ion tail seen in C III λ977. We present the observations, followed by a discussion of the atomic processes and a simple model for the Lyα intensity and velocity distributions. We then reconstruct images from the time series of long-slit spectra, and we derive elemental abundances and outgassing rates. Finally, we discuss the ion tail, and we compare the results with observations of other comets near the Sun.

2. Observations

The UVCS is described by Kohl et al. (1995). Its 41′ long entrance slit can be placed at heliocentric distances between 1.4 and 10 $R_\odot$ at any selected position angle. For this set of observations, we used the O VI channel and 50μ, 100μ, or 150μ slit widths, which provide 0.2, 0.4, or 0.6 Å spectral resolution and cover 14″, 28″, or 42″ spatial elements, respectively. The data were binned by different factors for the different observations, which reduces the spatial and spectral resolution in some cases. The O VI channel of the UVCS spectrograph includes a mirror that provides a redundant means of observing Lyα. Therefore, each spectrum covers two

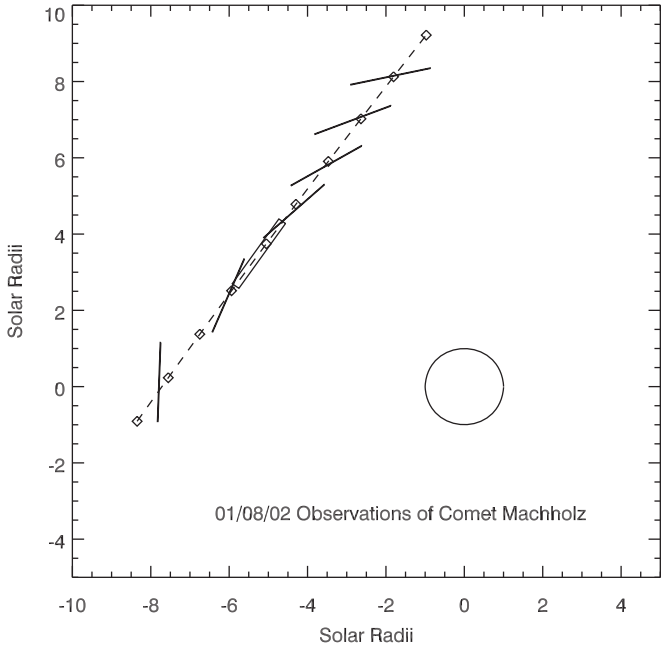

Figure 1. Positions of the UVCS slit for the seven crossings, progressing from the lower left to the upper right. The width of the slit for crossing 3, when the comet passed along the slit, is exaggerated. Diamonds indicate the comet position every 2 hr, from 01 UT in the lower left to 19 UT at the top.

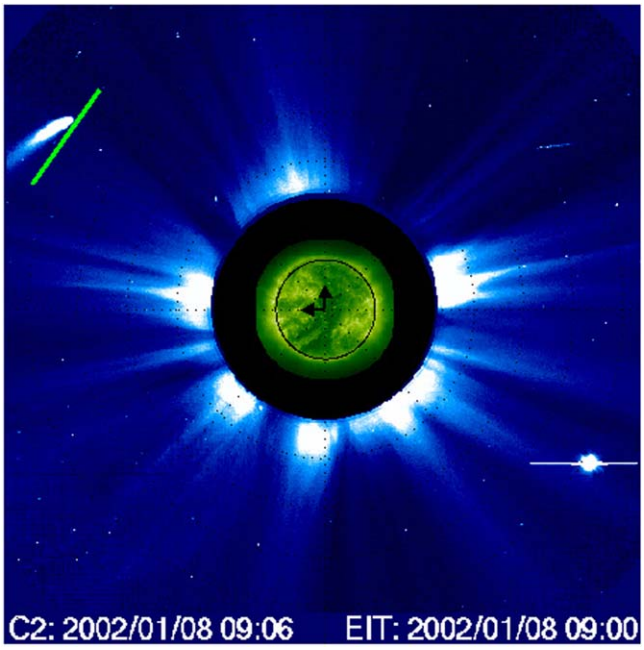

Figure 2. LASCO C2 image at the time of the third crossing at 6.27 $R_{\odot}$. The green bar indicates the slit position for the third crossing.

wavelength ranges, referred to as primary and redundant. The wavelength and radiometric calibrations are carried out for each channel separately in the UVCS data analysis software.

As with other comets observed by UVCS, the slit was placed so that Comet Machholz would drift across it over the course of 2–4 hr. Seven such crossings were observed over 16 hr. Different instrument configurations were used for the various crossings to obtain different spatial and spectral resolutions and ranges, trading those parameters off to stay within the data rate limitations imposed by the telemetry rate. Exposure times were 120 s, and about 10 s were needed for readout between exposures. For the third crossing, the slit was parallel to the comet's path so that the comet moved along the slit, providing many exposures and a high signal-to-noise ratio spectrum of the coma that is useful for faint lines.

The H I Lyα line is by far the brightest, and even when it does not fall on the detector (as in crossing 3), Lyα photons scattered by the grating generally dominate the noise level and impose the detection limit for faint lines. There are also a number of grating ghosts of the Lyα line that were identified in spectra of coronal mass ejections. Each of them has a fixed apparent wavelength and intensity ratio to Lyα. A noteworthy one at 1033 Å could be confused with an O VI line. We indicate those ghosts in the spectral plots, but we do not include them in tabulated spectra. The Lyα line is bright enough that it approaches the limit of linearity for the microchannel plate crossed delay line detector. We have used the correction given by K. Wilhelm in the SolarSoft package for the SUMER detector, which is virtually identical to that used by UVCS. The correction turned out not to be significant.

The slit positions are shown in Figure 1. Table 1 lists the slit position (apparent heliocentric distance, R, and position angle, PA) and primary and redundant spectral ranges for each slit crossing, along with the true heliocentric distance, r, and phase angle, α, from the ephemeris provided by Brian Marsden. Crossing 7 covered sections of the detector with four separate panels in a trade-off between resolution and spectral coverage. The wavelength ranges for each panel are given in Table 1.

Figure 2 shows the LASCO image taken at the time of the third crossing, with a green bar to represent the UVCS slit. During this exposure sequence, the comet nucleus moved along the slit. We measured the spectrum of the coma by tracking the brightest pixel in Lyβ as the comet moved along the slit during this crossing. The pixel covers an area given by the slit width and the spatial binning of 10 pixels, or $21'' \times 70''$ on the sky. We averaged the first 30 exposures, which were obtained before the coma drifted to the edge of the slit. The O I lines at 1027.4 and 1028.2 Å are on the wing of the Lyβ line, and we subtracted a scaled Lyβ profile from a region far from the coma before measuring this pair of lines. The spectrum is shown in Figure 3, and the intensities are given in Table 2.

Table 2 also gives intensities for the ion tail. We extracted the spectra of the ion tail from crossing 6 in two ways. First, we tracked the three spatial bins that show C III emission as the comet crossed the slit and averaged 20 exposures to provide the maximum feasible number of counts. However, the averaging dilutes the intensity because the emission is brightest just after the coma passes across the slit. Therefore, we also present the intensities for the single brightest $21'' \times 70''$ bin.

3. Analysis

3.1. Atomic Processes

Photoionization rates were computed based on extreme-ultraviolet fluxes from the SEE instrument on the TIMED satellite (Woods et al. 2000). Fluxes were not available for the day of our observations, so we used the spectrum from one solar rotation later. The photoionization cross sections were taken from Reilman & Manson (1979). Table 3 gives the rates at perihelion, 0.1241 au, and they can be scaled to the other heliocentric distances. They are compatible with the photo-ionization rates used in comet studies over many decades, the

Table 1
UVCS Observations of Comet Machholz, 2002 January 8

Crossing	R ($R_\odot$)	PA (deg)	r (au)	α (deg)	No. of Exp.	t_{cross} (UT)	Slit Width (μ)	λ_{PRI} (Å)	λ_{RED} (Å)
1	7.72	88.2	0.1267	163.6	165	02:23	50	970–977	1213–1220
2	6.47	64.5	0.1252	166.5	54	06:47	50	1018–1120	1177–1270
3	6.27	55.4	0.1247	166.7	54	...	100	942–1043	1100–1193
4	6.45	41.9	0.1244	166.5	54	11:12	50	1018–1119	1177–1271
5	6.85	30.4	0.1242	165.5	54	13:05	50	1018–1119	1177–1271
6	7.44	20.5	0.1241	163.8	54	15:03	150	940–1041	1126–1193
7	8.22	12.4	0.1242	162.0	54	16:58	50	987–992	1198–1202
								969–975	1213–1219
								1026–1041	1153–1166
								1048–1053	

major uncertainty being the level of solar activity at the time of the observation.

Two other processes can affect the ionization state: collisional ionization by electrons and charge transfer. The electron density and temperature are not known within the ion tail, but we can consider neutral H atoms in the solar wind, taking reference values of $T = 4.0 \times 10^5$ K based on the cooling of the solar wind as it expands away from the corona and $n_e = 400$ cm^{-3} based on the typical mass flux at 1 au and an intermediate solar wind velocity. The inner parts of the expanding hydrogen cloud are likely to be shielded from the solar wind, but since the neutrals cross magnetic field lines, the outer regions are exposed to the wind. The other elements expand slowly away from the nucleus, and their ions are confined to the ion tail. The temperature in the ion tail must be at least 30,000 K as a result of the energy deposited by photoionization, and we use that value. The density is poorly known, but considering the carbon outgassing rate derived in Section 3.6, the velocity range discussed in Section 3.5, and the apparent tail diameter of about 5×10^5 cm, the electron density due to carbon ions alone is more than 100 cm^{-3}. Considering the electrons produced by ionization of other species, the total density must be around 1000 cm^{-3}, and we use that value for Table 3.

The rate of charge transfer of H I with solar wind protons is typically higher than the photoionization rate. The solar wind mass flux is fairly constant, near 3×10^8 cm^{-2} s^{-1} at 1 au (Wang 2010), so scaling to 0.124 au and multiplying by the cross section of 1.1×10^{-15} cm^2 (Schultz et al. 2008) gives 2.2×10^{-5} s^{-1}. The charge-transfer process produces neutral H atoms with the solar wind speed and velocity distribution. While such neutrals produce the Lyα tails of sungrazing comets in the static corona near the Sun, in the case of Comet Machholz at 0.124 au, they are severely Doppler dimmed and do not contribute significantly to the observed Lyman line intensities. If they did contribute, they would be distinguished by a blueshift and line width determined by the solar Lyα profile and the velocity distribution of the solar wind protons, or around 100 km s^{-1}. One other charge-transfer process may be important. Because the ionization potentials of H and O are nearly equal, the charge transfer between neutral H and O^+, along with its inverse, is relatively fast. The table gives the rate based on the Kingdon & Ferland (1996) cross section, a temperature of 30,000 K, and a neutral hydrogen density of 1000 cm^{-3}, as would be typical for a distance of 0.1 $R_\odot$ from the nucleus and an outgassing rate of 5×10^{29} s^{-1}. It is slow enough compared to the photoionization rate that it can be neglected.

We note, however, that compression and heating of electrons by the bow shock or plasma waves could increase the collisional ionization and excitation rates. Feldman et al. (2018) discussed signatures of collisional excitation and dissociation in the ALICE spectra of Comet 67P/Churyumov–Gerasimenko, and Cravens et al. (1987) used a three-temperature approximation to the electron distribution measured near Comet Halley by Gringauz et al. (1986) to compute ionization rates. In the case of Comet Machholz, the bow shock standoff distance is of order 10^8 cm, which is small compared to the UVCS resolution elements. Nevertheless, the high density in that small region might make collisional processes significant.

Table 4 gives the photoexcitation rates of the lines we observe. The line intensities at 0.124 au are given in 10^9 ph (cm^2 s)$^{-1}$ in a wavelength interval corresponding to 30 km s^{-1} for H and 3 km s^{-1} for the other ions. The scattering cross sections are inversely proportional to this assumed line width, so the width cancels out provided that the absorption profiles are narrow. The spectral fluxes at the line center for Lyα and Lyβ are based on TIMED/SEE fluxes, scaled from total flux to line center spectral flux with the formulae of Lemaire et al. (2015). The profile of Lyγ was not included in Lemaire et al. (2015), so we estimate the line shape from the figure in Curdt et al. (2001). The O I and C II values are peak fluxes from the Curdt et al. (2001) SUMER atlas for the quiet Sun, scaled from solar minimum to the time of observation based on the assumption that they scale with Lyβ. The C III and N III lines are formed at higher temperatures. We assume that the increase in Lyβ compared to solar minimum results from the presence of active regions, and we use the quiet Sun–to–active region contrast given by Vernazza & Reeves (1978) to estimate the fraction of the Sun covered by active regions. We then use the contrast between the quiet Sun and active regions in the C III and N III lines to scale by a factor of 1.6 from the peak SUMER fluxes of Curdt et al. (2001).

Table 4 also gives the populations of the lower states that can absorb photons if statistical equilibrium within the ground levels holds, for instance, for the $^2P_{1/2}$ and $^2P_{3/2}$ states of N III and the $^3P_2$, $^3P_1$, and $^3P_0$ states of O I. The oscillator strengths, f, for H I are from the NIST database (DOI:10.18434/T4W30F), those for O I are from Morton (1991), and those for C II, C III, and N III are from Tachiev & Froese Fischer (1999) and Liang et al. (2012) from the CHIANTI (Del Zanna et al. 2021) database. The scattering cross sections, q_{exc}, are

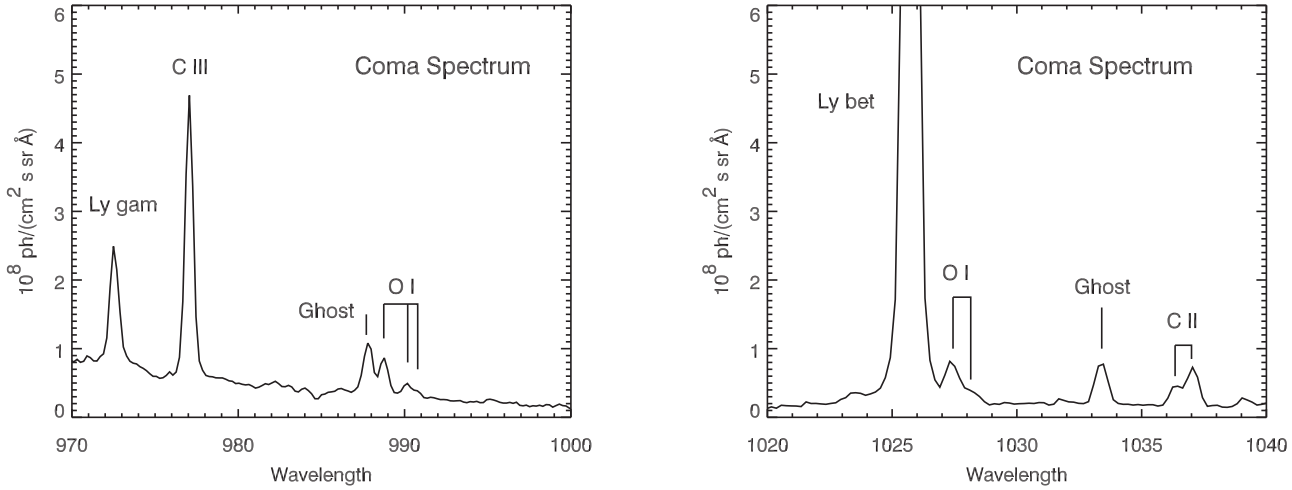

Figure 3. Spectrum of the coma. This is the average of the brightest 28″ × 70″ spatial bin over 40 exposures as the comet slid along the UVCS slit between 07:56 and 09:26 UT on January 8. Two grating ghosts are indicated, along with lines of H I, C II, C III, and O I. The continuum is due to Lyα photons scattered by the diffraction grating.

Table 2
Line Intensities 10^7 photons (cm^2 s sr)$^{-1}$

Ion	λ	Coma	Ion Tail Average	Ion Tail Peak
H I	1025.7	126.	4.55	16.8
H I	972.2	12.2	0.41	5.50
C III	1036.9	5.0	0.09	⋯
C III	977.0	25.1	1.21	11.9
N III	989,99	<1	<0.1	<1
O I	989.7	3.0	⋯	⋯
O I	991.0	1.8	⋯	⋯
O I	1027.4	2.9	⋯	⋯

Table 3
Ionization Rates at 0.1241 $R_\odot$

Ion	q_{phot} (s^{-1})	q_{coll}[a] (s^{-1})	q_{CT}[a] (s^{-1})
H I	4.47e-6	2.0e-5	2.2e-5
C I	7.70e-4	4.3e-7	
C II	9.56e-6	1.1e-9	
C III	1.85e-6	⋯	
N I	3.23e-5	7.5e-8	
N II	1.63e-6	1.9e-10	
N III	4.03e-6	⋯	
O I	4.04e-5	5.5e-8	1.16e-6

Note.
[a] See text for assumed density and temperature.

proportional to the oscillator strength, f, and branching ratios of 0.88 and 0.84 are included for Lyβ and Lyγ, respectively.

Because Comet Machholz was at perihelion, its velocity component toward the Sun was essentially zero, so Doppler dimming (reduction of the scattering rate when an atom is Doppler shifted away from the solar Lyα emission profile, somewhat analogous to the Swings effect) should not be significant. The plasma velocity within the ion tail is not independently known, however. Since the solar disk lines that illuminate the ions are fairly narrow, plasma speeds as low as 40 km s^{-1} could lead to significant Doppler dimming. We will return to this point in discussing the elemental abundances.

Table 4
Photoexcitation Rates at 0.1241 au

Ion	λ (Å)	$I_{.124}$[a]	Pop.	f	q_{exc} (s^{-1})
H I Lyα	1215.67	5240	1.0	0.416	0.22
H I Lyβ	1025.73	79.9	1.0	0.0791	5.4e-4
H I Lyγ	972.54	9.4	1.0	0.0290	4.4e-5
C II	1036.34	0.121	1.0	0.15	6.8e-5
C II	1037.00	0.141	1.0	0.15	1.6e-4
C III	977.03	1.39	1.0	0.76	0.0102
N III	989.82	0.049	0.33	0.12	1.9e-5
N III	991.59	0.092	0.66	0.12	7.0e-5
O I	988.75	0.033	0.55	0.051	1.0e-5
O I	990.19	0.022	0.33	0.051	4.0e-6
O I	990.79	0.011	0.12	0.051	6.9e-7
O I	1027.44	0.072	0.33	0.020	5.3e-6
O I	1028.15	0.032	0.11	0.020	7.8e-7

Note.
[a] $I_{.124}$ in 10^9 photons cm^{-2} s^{-1}.

Finally, we must consider the opacity in the Lyα line. For an outgassing rate of a few times 10^{29} s^{-1}, the optical depths between the nucleus and the Sun and between the nucleus and SOHO are each expected to be on the order of 1. We can assess the optical depth from the crossings that measured both Lyα and Lyβ intensities, since their ratio is constant for optically thin scattering. Crossings 2, 4, and 5 all showed an increase in the Lyβ/Lyα ratio by a factor of 2.2 close to the nucleus, meaning that Lyα was attenuated by a total optical depth (comet–Sun and comet–SOHO) of $\tau \approx 0.8$. The observations of these three crossings were highly binned in the spatial direction in order to give the broadest possible wavelength coverage, so that 0.8 is the weighted average of τ over a 14″ × 70″ spatial bin, or about 8600 × 43,000 km.

3.2. Water Production Rate

The H I Lyα radiance profiles of the comet obtained during the first and last crossings (1 and 7 in Table 1) through the UVCS slit were least-squares fitted to a Haser model with H atom velocities of 20 and 8 km s^{-1} (from photodissociation of

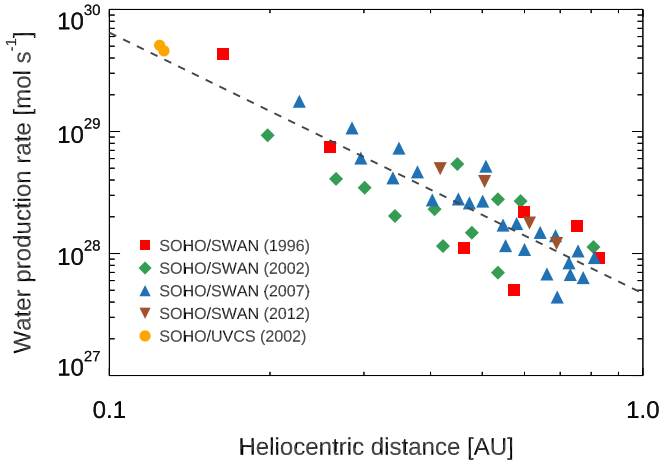

Figure 4. Water production rates in Comet Machholz plotted as a function of the comet's heliocentric distance. Shown are results from SOHO/SWAN observations obtained during four apparitions of the comet in 1996, 2002, 2007, and 2012 (Combi et al. 2011, 2019). The dashed line is an average power-law fit to the same data. The results obtained in this work near perihelion during two crossings of the UVCS slit (orange circles) are shown for comparison.

H_2O and OH, respectively). In the model, described by Mancuso (2015), the value for the lifetime τ_H of the H atoms was left as a free parameter, together with the unknown outgassing rate, Q_{H_2O}, to be solved by comparing the coma model with the Lyα radiance measured along the UVCS slit from the exposures containing the nucleus. The model was applied to the data by imposing the same value of τ_H for the two crossings. More details on the other assumed parameters can be found in Mancuso (2015). The best-fit Q_{H_2O} values estimated near perihelion for the two UVCS crossings are, respectively, 5.09×10^{29} and 4.58×10^{29} molecules s^{-1}, with a best-fitting $\tau_H = 1.5 \times 10^6$ s. However, that value of τ_H corresponds to a length scale above 10^{12} cm, which is much larger than the extent of the measured radiance profiles, and it is therefore uncertain. In Figure 4, we compare our results for Q_{H_2O} with the ones obtained by Combi et al. (2011, 2019) with SOHO/SWAN at larger heliocentric distances as part of the full-sky imaging program during the apparitions near perihelion of 1996, 2002, 2007, and 2012. An average power-law fit ($4.71 \times 10^{27}\, r(\mathrm{au})^{-2.14}$ molecules s^{-1}) to the SWAN estimates with respect to heliocentric distance is also superposed to the data. Despite the small perihelion distance and resulting activity, no apparent long-term decrease in Q_{H_2O} was evident over a decade. As is evident from visual inspection of Figure 4, the results obtained near perihelion with the two UVCS measurements are fully consistent with the ones estimated by SWAN at larger distances. The peak Lyα intensities were higher by 20%–30% in crossings 4 and 5, indicating a slight increase in the outgassing rate. Other complications, including optical depth in Lyα and the effects of radiation pressure on the H I atoms, are discussed below, and they might alter the inferred water production rate at the 20%–30% level.

3.3. Emission Models

To aid in interpreting the observations, we constructed models of the Lyα intensity and average velocity as seen from SOHO. Hydrogen atoms produced by photodissociation of H_2O and OH receive some kinetic energy, and most have initial speeds of 8–24 km s^{-1}. In the frame of the comet, they form a slowly expanding cloud, which we assume to be spherical. The atoms are destroyed by photoionization or collisional ionization at the rates given in Table 3. They also undergo charge transfer with solar wind protons, in which case they have the solar wind velocity and effectively cease to scatter Lyα photons due to Doppler dimming (the Swings effect). Thus, there is an exponential cutoff at a timescale of about $t_{cut} = 2.7 \times 10^4$ s, which corresponds to a spatial scale somewhat below 1 $R_\odot$. That is similar to the extent of the measured Lyα cloud.

Radiation pressure accelerates the H atoms, and the scattering rate in Table 4 implies an acceleration of 73 cm s^{-2}. In fact, the radiation pressure acceleration is comparable to the gravitational acceleration, just as for the micron-sized dust grains that are seen as the optical tail. Of course, the dust grains last much longer, and the range of sizes produces a range of ratios of radiative to gravitational forces. The main difference is that the H atoms are ejected at speeds an order of magnitude faster than the dust grains, so radiation pressure has a correspondingly smaller effect.

Given the initial speed and the acceleration, each atom follows an analytically described path relative to the nucleus. For a given initial speed, we eject particles at 1° intervals in altitude and azimuth about the axis pointing toward the Sun. Each particle scatters Lyα photons at the rate given in Table 4 multiplied by $\exp(-t/t_{cut})$ to account for the destruction of the H atoms. The optical depth in Lyα can be significant, so we use the computed density of H atoms to calculate the optical depth between each point and the Sun and multiply the emissivity by $\exp(-\tau)$. For the optical depth calculation, we approximate the velocity profile as a top hat with a width of twice the initial speed. This is somewhat crude, but the optical depth is only significant close to the nucleus for the outgassing rate of Comet Machholz.

The emission is computed in a $501 \times 501 \times 501$ grid of cells of 7″ as seen from SOHO, which was 0.86 au from the comet during the first crossing. The 3D model was then rotated to match the SOHO point of view. Because the phase angle was in the range 162°–167° during these observations, the line of sight is not far from the vector between the comet and the Sun. Therefore, the radiation pressure accelerates atoms toward SOHO.

We then sum the emission along each line of sight to produce a 2D model of the Lyα intensity, and we average the velocity to predict the velocity centroids as a function of distance from the nucleus. Figure 5 shows the predicted intensity image for an initial speed of 16 km s^{-1}. While the contours are approximately circular, the outer contours are displaced somewhat away from the Sun relative to the nucleus.

Though the hydrogen atoms follow different trajectories depending upon their initial velocities, the basic expectation is that they will be accelerated to speeds of order 20–30 km s^{-1} away from the Sun as they travel a distance of order 1 $R_\odot$ from the nucleus. Because our line of sight is not far from the comet–Sun line, most of that velocity will appear as a blueshift that gets stronger with distance from the comet. Figure 6 shows the velocity centroid as a function of distance from the nucleus measured during the first slit crossing. It is compared with the prediction of the model for a cut through the nucleus at an angle of 30°, approximately the angle between the comet's trajectory and the slit. This model assumed that H atoms leave the coma at 16 km s^{-1}.

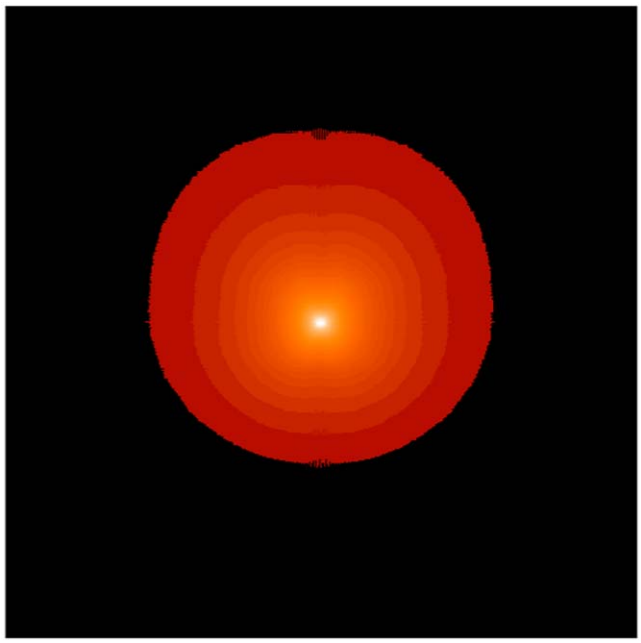

Figure 5. Simulation of the Lyα intensity as seen from SOHO. The intensity image is saturated near the nucleus in order to show the brightness at larger distances. The image is 3500″ (about 3.5 $R_\odot$) on a side. Note that although the image appears fairly round, the outer contours are shifted upward relative to the nucleus due to radiation pressure on the hydrogen atoms.

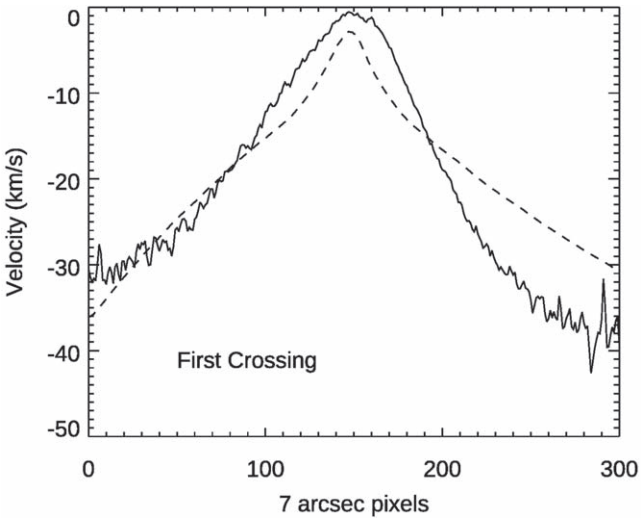

Figure 6. Observed velocity centroid relative to the centroid at the nucleus as observed during the first crossing (solid line). The dashed line is the prediction of the model.

The predicted velocity profile clearly leaves something to be desired. The motion of the comet during the three exposures that were averaged can account for some, but not all, of the discrepancy near the peak. Some of the discrepancy results from smoothing of the observations near the nucleus by the UVCS instrument profile at the fairly extreme grating position used here. We do not have exact figures, but we believe that the profile is smoothed by as much as 70″ in the spatial direction. In addition to the sharper peak of the predicted profile, the velocity centroid falls off too slowly as a function of distance ahead of the nucleus. A smaller initial speed would help somewhat, but that would cause the intensity to drop too quickly behind the nucleus.

There are serious limitations to the simple model. In particular, we assume that all of the hydrogen atoms are isotropically ejected at velocities of 16 km s^{-1}, while the speeds range from about 8 to 24 km s^{-1}. In addition, our treatment of optical depth effects is crude, and that will affect the line profile near the nucleus. Nevertheless, Figure 6 does show a zeroth-level agreement in that there is a blueshift of about 30 km s^{-1} at distances of about 150 pixels or about 1 $R_\odot$ from the nucleus. With the help of more sophisticated models, it might be possible to constrain the initial velocity distribution of the H atoms. In particular, if the H atoms lose very much momentum to heavier atoms such as O by collisions during the initial expansion, that would imply longer times to reach 1 $R_\odot$ from the nucleus and blueshifts larger than those observed. At the high outgassing rates inferred above, the H atoms are expected to lose a considerable amount of momentum on collisions with oxygen (Combi & Smyth 1988). Perhaps low-velocity H atoms contribute to the region of small Doppler shifts near the nucleus seen in Figure 6.

3.4. Reconstructed Images

We reconstruct intensity images with the method used for past UVCS observations of comets (Povich et al. 2003; Bemporad et al. 2005; Giordano et al. 2015), in effect using the motion of the comet across the slit as though we were making a raster scan of the slit across the comet. For each exposure, we measure the intensity of a line in each spatial bin along the slit and place it in a 2D array. The velocities of the comet perpendicular and parallel to the slit are known from the comet's orbit and the position angle of the slit. We multiply those velocities by the time between exposures (exposure time plus readout time, or about 130 s) and offset the intensities from subsequent exposures accordingly.

Figure 7 shows the composite LASCO images and reconstructed Lyα images from UVCS spectra at crossings 1, 2, 5, and 7, when Lyα was detected. Those images allow the comparison of the shape and orientation of the comet. The Lyα cloud is approximately, but not exactly, spherical, as predicted by the model in the previous section. A similar departure from spherical expansion was seen in reconstructed Lyα images of Comet Encke (Raymond et al. 2002). Figure 8 shows a larger version of the Lyα image from the first crossing, with contours indicating the intensity.

3.5. Ion Tail

A notable feature of the reconstructed images is the ion tail in C III λ977 emission seen in Figure 9. A similar C III tail was found in images reconstructed from UVCS spectra in Comet Kudo–Fujikawa (Povich et al. 2003). In that case, the ion tail was interrupted, apparently as a result of a disconnection event caused by interaction with a reversal in the direction of the interplanetary field (Brandt & Snow 2000). The image of the ion tail of Comet Machholz as seen from SOHO is foreshortened by about a factor of 2.4 because our line of sight is not far from the comet–Sun line. The angle between the C III tail and the comet trajectory is roughly 70°. Assuming that material in the tail moves radially away from the Sun, and correcting for the projection due to the viewing angle, the angle between the tail and the comet's path implies a velocity of the material in the tail of about 100 km s^{-1}. That is in line with Scherb et al. (1990) and Rauer & Jockers (1993), who

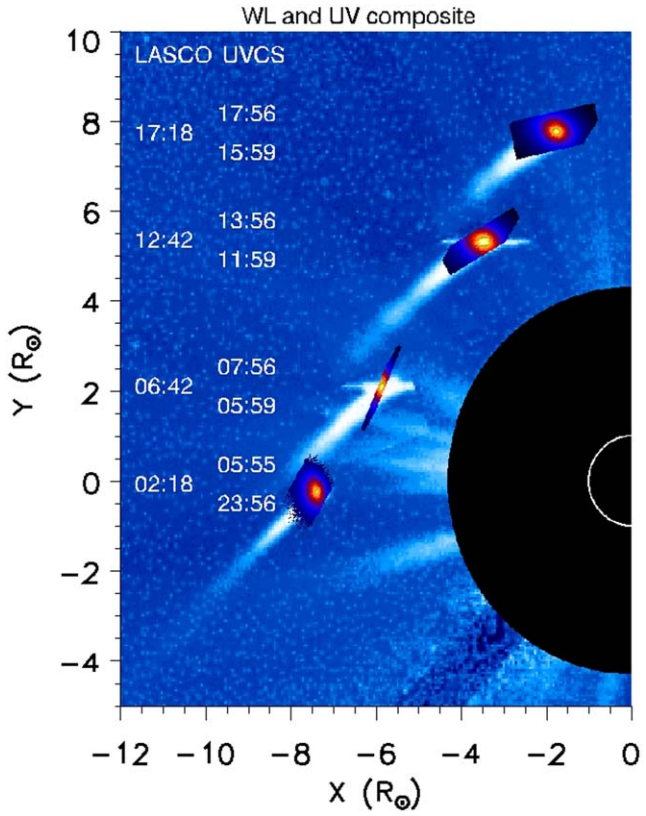

Figure 7. Composite comet image of visible light from LASCO C3 and reconstructed H I Lyα intensity from UVCS spectra. The labels report the observation times of LASCO C3 and the time interval of the UVCS observation.

measured Doppler shifts increasing to 70 km s^{-1} for H_2O^+ ions along the tails of comets Halley and Levy 1990c, respectively. It is also in line with Jockers et al. (1972), who found that the motions of features along the plasma tail of Comet Tago–Sato–Kosaka 1969 IX increased from 40 km s^{-1} close to the comet to 300 km s^{-1} farther away. Unfortunately, we cannot directly measure the velocity by means of the Doppler shift because of the 150μ slit width used for this observation and the uneven filling of the slit, which can shift the line centroid to the red or blue during different exposures.

An important consequence of the acceleration of C III ions to speeds above 50 km s^{-1} is severe Doppler dimming. The C III line from the disk is only about 50 km s^{-1} wide FWHM (Feldman et al. 2011). The width of the C III velocity distribution in the tail is difficult to measure because of the large slit width, but FWHM $<$ 120 km s^{-1} is an upper limit. Acceleration of the plasma along the ion tail could strengthen the Doppler dimming and cause the observed fading with distance from the nucleus. However, the fraction of carbon in the form of C III is very small near the nucleus (see Table 5 below) and apparently much larger in the tail, judging by the C III/C II ratio (Table 2). That offsets some of the effect of Doppler dimming. Some kinetic heating of the C III ions by the process that accelerates the plasma tail could also reduce the Doppler dimming effect.

3.6. Elemental Abundances

The elemental abundances are of special interest because of the unusually low C_2 and C_3 abundances relative to NH_2 in Comet Machholz (Langland-Shula & Smith 2007; Schleicher 2008).

Abundance analyses of sungrazing comets observed by UVCS yield total abundances because dust grains rapidly sublimate close to the Sun (Kimura et al. 2002). At 0.124 au, however, the sublimation times are longer, so the spectra of Comet 96/P Machholz reveal the composition of the volatile component. The intensities observed in the coma in Table 2 can be multiplied by 4π and divided by the photon scattering rates in Table 4 to obtain the column densities of the atoms and ions observed. The line-of-sight depth can be estimated from the size of the spatial element. Dividing that into the column density gives the density. We take the line-of-sight depth to be the average of the long and short dimensions of the $21'' \times 70''$ spatial element at a distance of 0.86 au, or 2.8×10^9 cm. Finally, multiplying by the outflow speed and 4π gives the outgassing rate. We present those rates in Table 5 separately for each line to provide a consistency check. We assume outflow speeds of 15 km s^{-1} for H and 3 km s^{-1} for the other elements.

The C/O ratio is probably the most reliable because C and O atoms should have similar velocities as they leave the coma. The O/H ratio is more questionable because the O and H velocities are different (Combi & Smyth 1988), and both are uncertain. In addition, the H abundance determined from Lyα is subject to optical depth uncertainty, and it may be affected by radiation pressure on the H atoms. The factor of 1.5 discrepancy in the rate of production of O determined from different O I lines may be due to uncertainty in the measured intensity of the lines at 1027 and 1028 Å, which are on the wing of the much brighter Lyβ line. However, one expects a hydrogen-to-oxygen ratio of 2:1, and the derived ratio is twice that. If CO or CO_2 contributes a significant amount of O, the discrepancy is made worse. The easiest explanation would be that the oxygen outflow rate is larger than we assumed.

Close to the nucleus, the carbon is mostly C II because C I is rapidly photoionized, and it takes so long to ionize C II to C III that only about 1% of the carbon in the central region is C III. Overall, we estimate the ratio of the outgassing rates of carbon and nitrogen as $\dot{N}(\mathrm{C})/\dot{N}(\mathrm{H}) \sim 0.02$. For comparison, the sungrazer C/2003 K7 showed $\dot{N}(\mathrm{C})/\dot{N}(\mathrm{H}) = 0.0006$–$0.018$, even with substantial dust sublimation at 3.37 $R_\odot$ (Ciaravella et al. 2010). We find that $\dot{N}(\mathrm{C})/\dot{N}(\mathrm{O}) < 1/10$ in Comet Machholz, suggesting that much of the carbon could be locked up in dust.

Unfortunately, $\dot{N}$(N) is poorly constrained because we have no N II lines and only an upper limit on N III. There is no obvious enhancement of nitrogen ions, which may be surprising in view of optical indications of strong NH_2 emission compared to C_2 and C_3. That might again indicate that much of the carbon remains locked in grains or is in the form of CO or CO_2.

We do not detect any Si lines, unlike in comets C/2011 W (Lovejoy) and C/2003 K7 (Ciaravella et al. 2010; Raymond et al. 2018). That is probably due to the fact that Comet Machholz was beyond the heliocentric distance where silicate grains can rapidly sublimate, and it is likely that nearly all of the silicon is in grains.

As noted in Section 3.1, collisional excitation and ionization could contribute to a degree not included in our estimates. However, the scale of the bow shock region where such processes will be strong is roughly $1''^2$, compared with a spatial resolution element of $1400''^2$ for crossing 3.

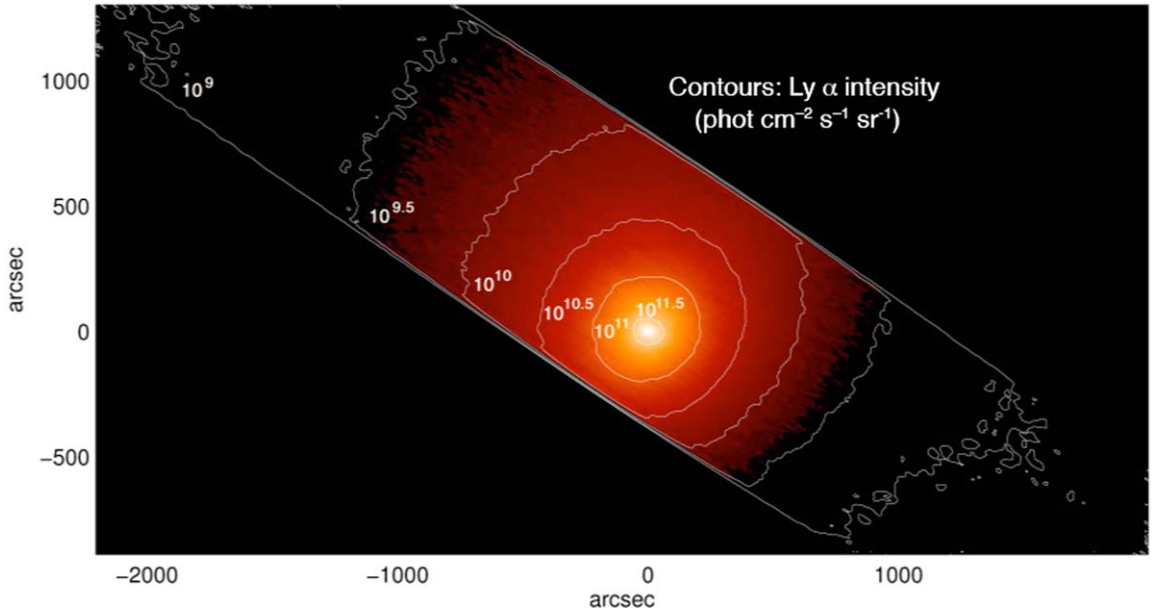

Figure 8. Reconstructed image in H I Lyα from the first crossing. Contours indicate the intensity.

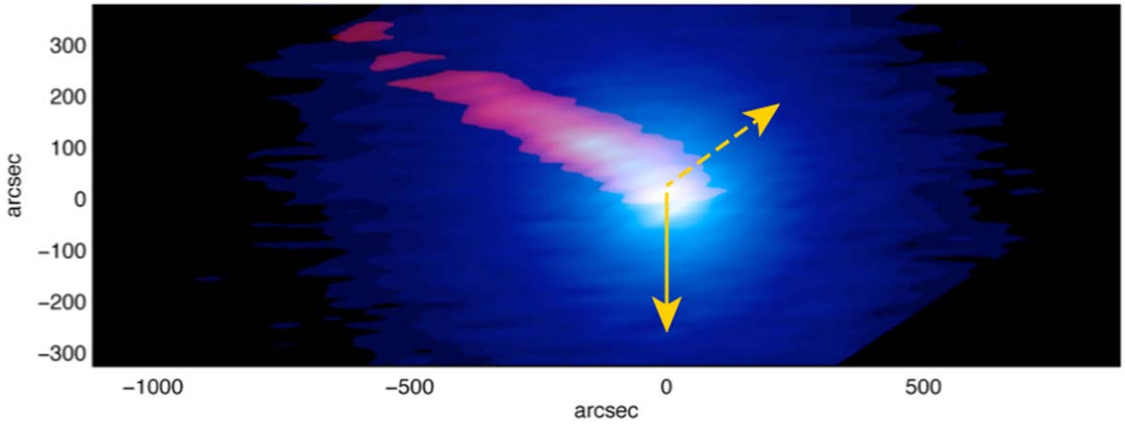

Figure 9. Reconstructed images in C III and H I Lyβ superposed in red and blue. The Lyβ image shows a nearly spherical cloud expanding away from the nucleus, while C III shows the ion tail. This image demonstrates the spatial relationship. The solid arrow points toward the Sun, and the dashed arrow points along the comet trajectory. The striations are due to variations in the detector sensitivity.

Table 5
Coma Column Densities and Outgassing Rates

Ion	λ (Å)	N (10^{12} cm^{-2})	n (cm^{-3})	$\dot{N}$ (10^{28} s^{-1})
H I Lyβ	1025.73	29.0	10,400	38.0
H I Lyγ	972.54	35.0	12,300	45.0
C II	1036, 1037	2.8	992	0.73
C III	977.03	0.31	110	0.008
N III	989, 990	<1.4	<510	<0.37
O I	988.75	38.0	13,600	10.0
O I	990, 991	47.0	16,800	12.4
O I	1027, 1028	58.0	21,000	15.7

4. Discussion

As described in Section 3.2, the outgassing rate fits nicely with the extrapolation of the values determined by Combi et al. (2011, 2019) at larger distances.

The UVCS has observed two other short-period comets, Comet 2P/Encke (Raymond et al. 2002) and Comet C/1997 H2 (Mancuso 2015), both near perihelion at 0.34 and 0.137 au, respectively. Comet 2P/Encke showed an outgassing rate of 1.1×10^{29} H atoms s^{-1}, increasing by about 30% over the course of a day. The upper limits on the O I and C II lines were about 10^{-4} times Lyα. That is consistent with the Comet Machholz observations, except for the C III line, which is 3×10^{-4} times as strong as Lyα in the nucleus but probably consistent with 10^{-4} when averaged over a larger volume. Comet Encke's Lyα brightness contours showed a small deviation from spherical, presumably due to radiation pressure as in Comet Machholz. Comet C/1997 H2 also had a similar outgassing rate of 1.2×10^{29} H atoms s^{-1}.

Comet 2002/X5 (Kudo–Fujikawa) was a longer-period object that was observed near perihelion at 0.19 au (Povich et al. 2003). It showed much higher outgassing rates of 1–5.4×10^{30} H atoms s^{-1} and carbon-to-hydrogen ratios of order 20% based on submillimeter observations of carbon-bearing molecules (Biver et al. 2011), as opposed to 2% in Comet Machholz. Comet Kudo–Fujikawa would be an older long-period comet according to the classification of

A'Hearn et al. (1995), so it has probably passed through the inner solar system before. Perhaps the most interesting similarity between Comet Kudo–Fujikawa and Comet Machholz is the ion tail observed in the C III emission line. The two comets were observed close to the Sun, and that is probably necessary for the ionization of C II to C III over a modest length scale. Povich et al. (2003) obtained two reconstructed images of the ion tail of Comet Kudo–Fujikawa. The first image shows a disconnection event that was attributed to the crossing of a field reversal in the solar wind (Brandt & Snow 2000). The second image resembles that seen in Comet Machholz in curvature and length but viewed from a different angle.

Emission from carbon ions has also been detected in the sungrazing comet C/2003 K7 (Ciaravella et al. 2010), which showed a C:H ratio of about 0.004. That comet was observed at a heliocentric distance of 3.4 $R_\odot$, which meant that grains were very rapidly sublimated, and the abundance ratio includes both gaseous and dust components. Nevertheless, Comet Machholz shows a much higher C:H ratio of about 1.8%. Comet C/2003 K7 was a member of the Kreutz family of sungrazing comets, and it was close enough to the Sun that it had been reduced to its inner core by the time of the observation. Its small carbon abundance might be a feature of the Kreutz family, or it could indicate composition variation between the center and surface of the original comet.

5. Summary

Comet Machholz is unusual in many ways, including its orbit (Green et al. 1990; McIntosh 1990), its relationship to the Marsden and Kracht groups of sungrazing comets (Ohtsuka et al. 2003), and its low apparent C:N ratio (Langland-Shula & Smith 2007; Schleicher 2008).

The UVCS observations during the 2002 perihelion show outgassing in agreement with values extrapolated from SWAN measurements at larger radii (Combi et al. 2011). The H I Lyα cloud that expands slowly away from the comet nucleus is affected by radiation pressure on the hydrogen atoms, producing a modest asymmetry and about 30 km s^{-1} Doppler shifts when seen from the point of view of SOHO. The ion tail is seen in C III, and it is similar to that seen in Comet Kudo–Fujikawa (Povich et al. 2003). We do not have useful measurements of the Doppler shift, but the intensity structure is consistent with the gradual acceleration of the ion tails seen in molecular ions in other comets (Jockers et al. 1972; Scherb et al. 1990). The ratio of C to H_2O of 1.8% is not anomalously low, but we do not have a good limit on N, so the low C/N ratio seen in molecules (Langland-Shula & Smith 2007; Schleicher 2008) remains mysterious. Perhaps the carbon originated from CO or CO_2.

Geraint Jones and Matthew Knight predict that Comet Machholz will transit the Sun from the point of view of the Solar Orbiter in 2023 January. That will be an excellent opportunity for observations with the Metis coronagraph, since the white-light images will show the effects of scattering at extreme phase angles, and the Lyα images will show the Lyα cloud discussed here but projected at different angles. The images can be used to extract both solar wind and comet parameters (Bemporad et al. 2015). Other instruments on the Solar Orbiter should be able to observe the comet in absorption.

The authors gratefully acknowledge the contributions of Brian Marsden, whose orbit calculations made the UVCS observations possible, and the UVCS operations team that carried out the observations. We also thank the anonymous referee, who pointed out gaps in our knowledge of comets. This work was supported by NASA grant NAG5-12814 to the Smithsonian Astrophysical Observatory.

ORCID iDs

J. C. Raymond https://orcid.org/0000-0002-7868-1622
S. Giordano https://orcid.org/0000-0002-3468-8566
S. Mancuso https://orcid.org/0000-0002-9874-2234
Matthew S. Povich https://orcid.org/0000-0001-9062-3583
A. Bemporad https://orcid.org/0000-0001-5796-5653

References

A'Hearn, M. F., Millis, R. C., Schleicher, D. O., Osip, D. J., & Birch, P. V. 1995, Icar, 118, 223
Bemporad, A., Giordano, S., Raymond, J. C., & Knight, M. M. 2015, AdSpR, 56, 2288
Bemporad, A., Poletto, G., Raymond, J., & Giordano, S. 2007, P&SS, 55, 1021
Bemporad, A., Poletto, G., Raymond, J. C., et al. 2005, ApJ, 620, 523
Biver, N., Bockelée-Morvan, D., Colom, P., et al. 2011, A&A, 528, A142
Brandt, J. C., & Snow, M. 2000, Icar, 148, 52
Ciaravella, A., Raymond, J. C., & Giordano, S. 2010, ApJL, 713, L69
Combi, M. R., Boyd, Z., Lee, Y., et al. 2011, Icar, 216, 449
Combi, M. R., Mäkinen, T. T., Bertaux, J. L., Quémerais, E., & Ferron, S. 2019, Icar, 317, 610
Combi, M. R., & Smyth, W. H. 1988, ApJ, 327, 1044
Cravens, T. E., Kozyra, J. U., Nagy, A. F., Gombosi, T. I., & Kurtz, M. 1987, JGR, 92, 7341
Curdt, W., Brekke, P., Feldman, U., et al. 2001, A&A, 375, 591
Del Zanna, G., Dere, K. P., Young, P. R., & Landi, E. 2021, ApJ, 909, 38
Eisner, N. L., Knight, M. M., Snodgrass, C., et al. 2019, AJ, 157, 186
Feldman, P. D., A'Hearn, M. F., Bertaux, J.-L., et al. 2018, AJ, 155, 9
Feldman, U., Dammasch, I. E., & Doschek, G. A. 2011, ApJ, 743, 165
Giordano, S., Raymond, J. C., Lamy, P., Uzzo, M., & Dobrzycka, D. 2015, ApJ, 798, 47
Green, D. W. E., Rickman, H., Porter, A. C., & Meech, K. J. 1990, Sci, 247, 1063
Gringauz, K. I., Gombosi, T. I., Remizov, A. P., et al. 1986, Natur, 321, 282
Grynko, Y., Jockers, K., & Schwenn, R. 2004, A&A, 427, 755
Jockers, K., Lust, R., & Nowak, T. 1972, A&A, 21, 199
Jones, G. H., Knight, M. M., Battams, K., et al. 2018, SSRv, 214, 20
Kimura, H., Mann, I., Biesecker, D. A., & Jessberger, E. K. 2002, Icar, 159, 529
Kingdon, J. B., & Ferland, G. J. 1996, ApJS, 106, 205
Kohl, J. L., Esser, R., Gardner, L. D., et al. 1995, SoPh, 162, 313
Langland-Shula, L. E., & Smith, G. H. 2007, ApJL, 664, L119
Lemaire, P., Vial, J. C., Curdt, W., Schühle, U., & Wilhelm, K. 2015, A&A, 581, A26
Liang, G. Y., Badnell, N. R., & Zhao, G. 2012, A&A, 547, A87
Mancuso, S. 2015, A&A, 578, L7
Matlovič, P., Tóth, J., Rudawska, R., Kornoš, L., & Pisarčíková, A. 2019, A&A, 629, A71
McIntosh, B. A. 1990, Icar, 86, 299
Morton, D. C. 1991, ApJS, 77, 119
Ohtsuka, K., Nakano, S., & Yoshikawa, M. 2003, PASJ, 55, 321
Povich, M. S., Raymond, J. C., Jones, G. H., et al. 2003, Sci, 302, 1949
Rauer, H., & Jockers, K. 1993, Icar, 102, 117
Raymond, J. C., Downs, C., Knight, M. M., et al. 2018, ApJ, 858, 19
Raymond, J. C., Fineschi, S., Smith, P. L., et al. 1998, ApJ, 508, 410
Raymond, J. C., & Giordano, S. 2019, ApJ, 887, 45
Raymond, J. C., Uzzo, M., Ko, Y. K., et al. 2002, ApJ, 564, 1054
Reilman, R. F., & Manson, S. T. 1979, ApJS, 40, 815
Scherb, F., Magee-Sauer, K., Roesler, F. L., & Harlander, J. 1990, Icar, 86, 172
Schleicher, D. G. 2008, AJ, 136, 2204
Schultz, D. R., Krstic, P. S., Lee, T. G., & Raymond, J. C. 2008, ApJ, 678, 950
Tachiev, G., & Froese Fischer, C. 1999, JPhB, 32, 5805
Uzzo, M., Raymond, J. C., Biesecker, D., et al. 2001, ApJ, 558, 403
Vernazza, J. E., & Reeves, E. M. 1978, ApJS, 37, 485
Wang, Y. M. 2010, ApJL, 715, L121
Woods, T., Bailey, S., Eparvier, F., et al. 2000, PCEC, 25, 393